Mesoporous C-doped C_3N_5 as a superior photocatalyst for CO_2 reduction

Aathira M. Sadanandan [a], Mohammed Fawaz [a], Nithinraj Panangattu Dharmarajan [a,*], Matej Huš [b], Gurwinder Singh [a], CI Sathish [a], Blaž Likozar [b], Zhixuan Li [a], Ajanya M. Ruban [a], Chung-Hwan Jeon [c], Jae-Hun Yang [a,*], Prashant Kumar [a], Ajayan Vinu [a,*]

[a] Global Innovative Centre for Advanced Nanomaterials, School of Engineering, College of Engineering, Science and Environment, The University of Newcastle, NSW 2308, Australia
[b] National Institute of Chemistry, Department of Catalysis and Chemical Reaction Engineering, Hajdrihova 19, Ljubljana SI-1000, Slovenia
[c] PNU-UON Green Energy Ammonia Global-Hub Research Center, Pusan Clean Energy Research Institute and Pusan CFBC Research Center, Pusan National University, Busan 46241, South Korea

ABSTRACT

Use of naturally abundant solar light for CO_2 reduction is a green pathway to reduce carbon footprint. C_3N_5 is a promising visible-light photocatalyst with enhanced local electron concentration and more active N=N sites compared to g-C_3N_4. We herein report development of mesoporous C-doped C_3N_5 through a simple copolymerisation of 3-amino-1,2,4-triazole with trimesic acid via hard-templating method, which demonstrated enhanced light absorption ability and delocalised π-electron density (as evident from density functional theory calculation), resulting in efficient charge transfer to the active surface sites of the photocatalyst. The optimised C-doped mesoporous C_3N_5 exhibited a superior photocatalytic CO_2 reduction activity with the CO evolution of 116.6 μmol·g^{-1}, which is 4-fold and 12-fold times higher than that of C_3N_5 and g-C_3N_4 respectively. The enhanced photocatalytic CO_2 conversion efficiency can be attributed to the synergetic effects of π-electron modulation by C-doping and enhanced surface-active sites brought by mesoporosity.

1. Introduction

The pressing need of energy per capita in residential areas and in industries worldwide, has adversely impacted environment with greenhouse gas emissions, out of which CO_2 emission is a major one [1]. Global warming (average temperature rise of ~ 1 °C since the pre-industrial era) is one of the concerning outcomes leading to unpredictable climatic conditions, which world leaders want to contain within a limit as soon as possible [2]. The devastating consequences of climate change can be mitigated by effective conversion of CO_2 into value-added products [3–6]. Inspired by the natural phenomenon of photosynthesis, directly harnessing renewable and abundant solar energy for photocatalytic conversion of CO_2 to valuable products seems extremely promising and viable [7–9]. In this photocatalysis reaction, the electrons generated in semiconducting photocatalysts by absorbing sunlight facilitate the chemical reduction of CO_2 molecules to valuable chemicals, such as CO, CH_4, CH_3OH, COOH, etc., while an oxidation reaction takes place by photogenerated holes [10,11].

Numerous nanomaterials catalysts have extensively been explored for photocatalytic CO_2 conversion including TiO_2, metal complexes, and carbon nitride (CN), etc [12–14]. Among these materials, CN-based photocatalysts have attracted significant attention owing to the feasibility of mass production at economic cost, and their unique physicochemical properties such as visible-light harvesting capability, photostability, and high photoactivity [15,16]. The potentials of its conduction band (CB) minimum (~ −1.4 V) and the valence band (VB) maximum (~ +1.3 V) are significant enough to reduce CO_2 and oxidize water, respectively, under visible light irradiation [17,18]. However, despite these advantages, CN-based photocatalysts still exhibit low conversion efficiency owing to the rapid recombination of charge carriers in CN, and limited absorption of broad visible light [19]. To address this limitation of g-C_3N_4, several strategies including doping by heteroatoms, and hybridization with other semiconductors, and metal complexes have been developed, leading to enhanced light absorption and dampening of the exciton recombination kinetics [20]. Additionally, the stoichiometric nitrogen content can be tuned using N-rich

precursors, and the resulting N-rich CNs (e.g. C_3N_5 having $E_g \sim 2$ eV) exhibit enhanced visible light absorption and the local electron concentration at the edge N atoms near the crystal defects act as catalytically active sites necessary for CO_2 conversion [21]. Additionally, it demonstrates a low Gibbs free energy for CO_2 reduction compared with H_2 production, indicating that CO_2 reduction is more favourable than H_2 evolution [22]. Moreover, the ring size and pore size of C_3N_5 are larger than those of g-C_3N_4 due to the presence of multiple π-bonded N atoms within the C_3N_5 structure. These unique properties facilitate the efficient adsorption of the COOH* intermediate and the subsequent CH_4 evolution as a final product in photocatalytic CO_2 reduction [22]. However, there have been limited reports on photocatalytic CO_2 reduction using N-rich CNs due to the fast kinetics of electron-hole recombination and low conductivity [21].

Keeping an eye on the urgency to develop superior performance solar-active photocatalyst and also the feasibility of mass production at industrial scale, we developed a mesoporous C-doped C_3N_5 (MCN-TMA-x) synthesized through the simple copolymerization of 3-amino-1, 2, 4-triazole with trimesic acid (TMA) via a hard-templating method for enhancing the photocatalytic CO_2 conversion activity. The local electronic structure and functional groups of MCN-TMA-x were analysed using advanced characterisation techniques such as FTIR, NEXAFS, and XPS. Additionally, textural and porosity studies were conducted using HR-TEM, BET, and SEM techniques. Theoretical calculations were performed by the density functional theory (DFT) and time dependent DFT to understand the possible structure of the catalyst and its performance under illumination. The enhanced photocatalytic activity can be attributed to the synergistic effect of numerous active sites, modified band structure by C-doping, suppressed electron-hole recombination rate, and high specific surface area of the mesoporous C-doped C_3N_5. The developed carbon substituted N-rich CN-based photocatalyst would be a promising catalyst to produce valuable chemicals from CO_2 via artificial photosynthesis.

2. Experimental section

2.1. Materials used

Chemicals such as 3-Amino-1,2,4-triazole ($C_2H_4N_4$, 95 %), trimesic acid (95 %), and LUDOX® HS-40 colloidal silica (40 wt% in H_2O) were acquired from Sigma Aldrich and used without additional purification. Deionised water was used in all experiments.

2.2. Synthesis of mesoporous carbon-doped C_3N_5 (MCN-TMA)

3 g of 3-amino-1,2,4-triazole (3-AT) and x amounts of trimesic acid (TMA) were dissolved in 50 mL of deionized water by sonication, where x was 0, 3, 6, 15, and 30 mg. The solution was then transferred to a Teflon-lined autoclave and heated in a hot-air oven at 170 °C for 10 h. The resulting solution was mixed with 2.5 g of HS-40 Ludox colloidal silica (particle size = 12 nm) as a hard template. The mixed suspension was evaporated at 65 °C under stirring to obtain a dried powder. The collected white powder was ground in an agate mortar, followed by calcination in a ceramic crucible with a lid at 500 °C for 4 h at a ramp rate of 2.5 °C/min in a muffle furnace under N_2 atmosphere at a flow rate of 7.5 L/min. The silica template in the resulting brownish sample was removed by washing with 5 wt% HF (aq) and further washed with water and ethanol. The collected samples were dried at 100 °C for 12 h and denoted as MCN-TMA-x, where x indicates the amount of TMA, such as MCN-TMA-0, MCN-TMA-3, MCN-TMA-6, MCN-TMA-15 and MCN-TMA-30. For comparison, bulk C_3N_5 was synthesized by pyrolyzing 3 g of 3-AT at 500 °C for 4 h with a ramp rate of 2.5 °C/min under a N_2 atmosphere with a flow rate of 7.5 L/min according to the previously reported method [17]. The resulting light brown sample was collected and ground, which was denoted as C_3N_5.

2.3. Materials characterisation

XRD measurements were performed using a Panalytical Empyrean X-ray diffractometer 9XRD) equipped with Cu-Kα radiation (λ = 1.5418 Å) and Galipix 3D Detector operating at 40 kV and 40 mA. FT-IR spectra were recorded with a Frontier FT-IR spectrometer (Perkin Elmer) using the KBr disk method over the wavenumber range 400–4000 cm^{-1}. Transmission electron microscopy (TEM) analysis was performed using JEM-2100 TEM (Jeol). Scanning electron microscopy (SEM) images were obtained using JSM-7900F FE-SEM (Jeol) after Pt coating to minimize the electron charging effect. Near-edge X-ray absorption fine structure (NEXAFS) analysis was performed using the Soft X-ray Spectroscopy Beamline at the Australian Synchrotron. The X-ray photoelectron spectroscopy (XPS) was collected using monochromatized Al Kα radiation for detailed chemical analysis. UV-Vis spectra of the powder samples were collected using a Lambda 1050+ UV-Vis spectrometer with an integrating sphere (Perkin Elmer). The N/C elemental ratios of the samples were evaluated using an EA 2400 elemental analyser (Perkin Elmer). To analyse the porosity, such as the specific surface area, pore volume, and size distribution, N_2 adsorption-desorption isotherms for the samples were recorded at liquid nitrogen temperature using ASAP 2040 (Micrometrics) after degassing the samples under vacuum (10^{-3} Torr) at 200 °C for 12 h. The specific surface area and pore-size distribution were calculated using the Brunauer–Emmett–Teller (BET) and–Barrett–Joyner Halenda (BJH) methods, respectively.

2.4. Photocatalytic CO_2 reduction

The photocatalytic CO_2 reduction reaction was performed using a laboratory-designed closed-circulating system. The prepared photocatalyst (30 mg) was dispersed in 11 mL of an organic–aqueous solution containing 9 mL acetonitrile, 1 mL water and 1 mL triethanolamine (TEOA) in a top irradiation reactor. 5 μmol of $Co(bpy)_3^{2+}$ was added into the suspension as a co-catalyst. The reactor was evacuated to remove all unwanted gases, such as N_2 and O_2, and was filled with CO_2/Ar mixed gas (60 % CO_2) at 760 Torr. Then, the photocatalytic reaction was conducted under 300 W Xe lamp (Newport) equipped with a 400 nm cut-off filter (λ ≥ 400). The reaction temperature was maintained at 15 °C by using a cooling chiller. The evolved gaseous products were in-situ analysed at every hour with the connected Pekin Elmer GC equipped with FID and TCD detectors and a stainless-steel column packed with Hay-eSep D.

2.5. Electrochemical measurements

For the fabrication of the working electrode, 50 mg of the sample was mixed with 50 μL of 10 wt% Nafion and 200 μL of ethanol and ground further to achieve a homogenous slurry. The prepared slurry was coated on 1 cm^2 masked FTO glass via a doctor blade technique and dried at room temperature. The exposed FTO surface was covered with epoxy resin to prevent direct contact between FTO and the electrolyte. 0.2 M Na_2SO_4 (aq) electrolyte solution was used for electrochemical measurements, such as Mott-Schottky measurements and electrochemical impedance spectroscopy. The data were recorded via a three-electrode system using a CHI760 electrochemical workstation, where platinum wire, Ag/AgCl (3 M KCl), and a photocatalyst-coated electrode were used as the counter, reference, and working electrodes, respectively. Electrochemical experiments commenced after purging with Ar gas for 20 min to remove oxygen or any other gas adsorbed on the sample surface or in the solution. For Mott Schottky measurements, the potential was scanned in the range of 0.3 V to 1 V (vs. Ag/AgCl and further converted to potential vs. NHE), and the electrochemical impedance spectrum (EIS) was recorded by stepping up the frequency from 100 KHz to 10 mHz with a 10 mV AC excitation signal. The photocurrent was recorded at zero potential (vs Ag/AgCl electrode) by irradiating a visible light (λ ≥ 400) on the non-conductive side of the working electrode.

2.6. Theoretical calculation insights for CO_2 reduction

For the better understanding of the photocatalyst for the photocatalytic CO_2 reduction into value added products, computational studies were investigated. Theoretical calculations were carried out with VASP 6.3.1, which is a periodic plane-wave code [23–25] using the projector augmented-wave method [26]. Preliminary testing showed that a 4x4x1 sampling of K-points centered around the gamma point sufficed for well converged results. A kinetic energy cutoff of 500 eV was used. A one-layered C_3N_5 structure and the C-doped varieties were optimized with a PBE functional [27] with a force threshold of 0.01 eV/Å. To account for the weak binding of CO_2 through the van der Waals forces, a Grimme D3 correction was used [28]. While the PBE energies sufficed for the calculations of energetics, electronic structures (HOMO and LUMO, band gaps) were assessed at the hybrid level with a HSE06 functional [29]. Spin polarization was included when required (i. e., non-paired electrons were present in the unit cell). Ground state energetics were described with DFT calculations, while for the excited state, time-dependent DFT (TD-DFT) was used, and the first excited state was considered, as justified by Kasha's rule. In the analysis of the reaction mechanism, the most favourable sites for the adsorption of different intermediates were used. For the TD-DFT calculations, no geometric optimization was performed.

3. Results and discussion

MCN-TMA-x was successfully synthesized by pyrolyzing (500 °C,

4 hours) 3-amino-1,2,4-triazole and trimesic acid assisted by the hard template method using HS-40 Ludox colloidal silica template, as illustrated in Fig. 1a. The mesoporous nature and porosity parameters, such as the specific surface area and pore size distribution, were analysed by N_2 adsorption-desorption isotherms, which are displayed in Fig. 1b and Fig. S1 and summarized in Table S1. BJH pore-size distribution curves calculated from the adsorption isotherms for C_3N_5, and MCN-TMA-x were plotted in Fig. 1c. MCN-TMA-0 demonstrated enhanced adsorption properties with a typical Type IV adsorption curve, revealing the formation of mesopores in N-rich carbon nitride. The BET-specific surface area (SSA) and total pore volume of MCN-TMA-0 were determined to be 69 m^2g^{-1} and 0.19 cm^3g^{-1}, which are significantly higher than those of C_3N_5 (8 m^2g^{-1} and 0.02 cm^3g^{-1}).

The material prepared by adding 6 mg of TMA in the precursor solution (MCN-TMA-6) also exhibited a similar N_2 adsorption-desorption behaviour, and its specific surface area and pore volume were 64 m^2g^{-1} and 0.19 cm^3g^{-1}, respectively, which were almost similar to those of MCN-TMA-0. However, with an increase in the amount of TMA to 30 mg (MCN-TMA-30), these values were reduced to 38 m^2g^{-1} and 0.10 cm^3g^{-1}. Based on the BJH pore size distribution analysis, the pore sizes of both MCN-TMA-0 and MCN-TMA-6 were determined to be approximately 12 nm, as shown in Fig. 1c, which closely matched with the size of the SiO_2 colloidal particles (12 nm) used as the hard template in our experiment. This suggests that mesopores were successfully created through replication using the silica nanoparticle template. This finding is consistent with the results obtained from mesoporous g-C_3N_4 prepared from cyanamide or dicyanamide and silica nanoparticles [30].
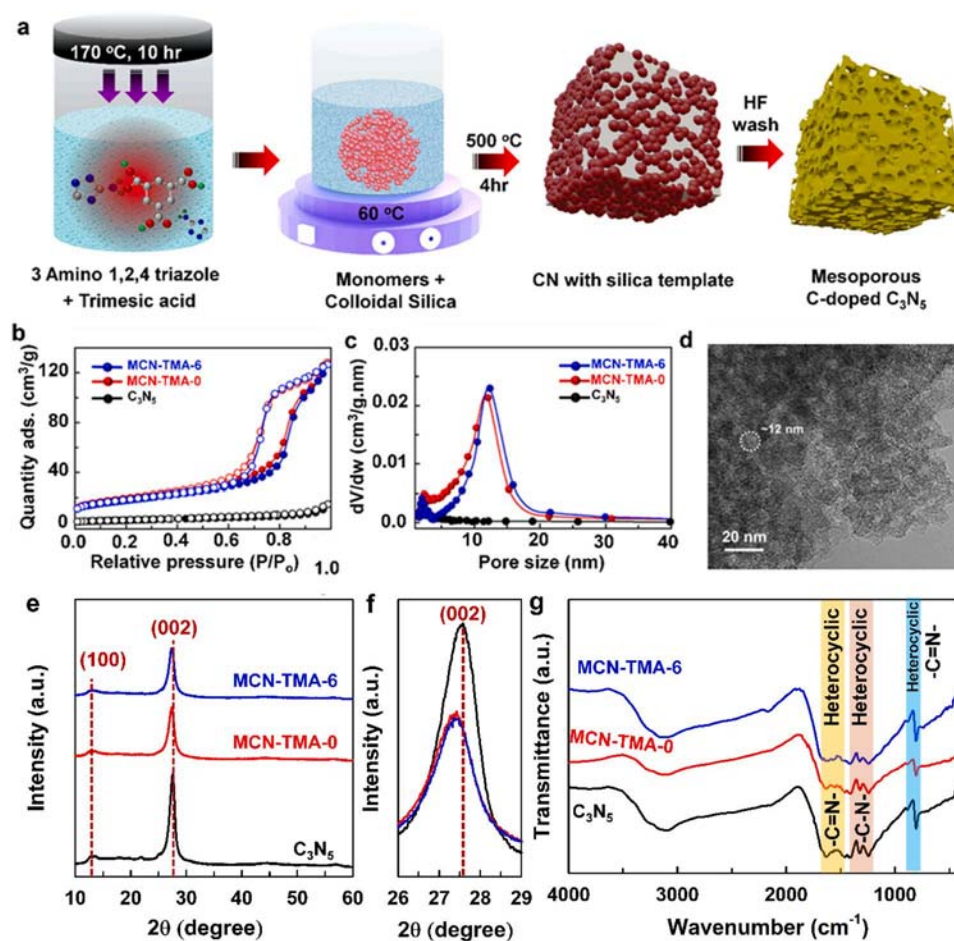

Fig. 1. (a) Schematic diagram showing synthesis of mesoporous C-doped C_3N_5 via hard templating approach; (b) N_2 adsorption-desorption isotherms and (c) pore size distribution of the prepared Bulk C_3N_5, MCN-TMA-0 and MCN-TMA-6; HR-TEM images of MCN-TMA-6, (d) enlarged view of the dashed square part image at 20 nm; (e - f) X-ray diffraction pattern, and (g) FTIR spectra of Bulk C_3N_5, MCN-TMA-0 & MCN-TMA-6.

These porous surfaces can act as adsorption and photocatalytic conversion sites of the CO_2 molecules [31].

The porous morphology characteristics of synthesized CNs were also confirmed by TEM analysis. C_3N_5 exhibited a stacked sheet-like morphology with a lateral size of ~ 600 nm (Fig. S2a). However, MCN-TMA-6 clearly demonstrated a porous texture in the TEM images (Fig. S2b and Fig. 1d). Furthermore, the pore size was found to be approximately 12 nm, which is consistent with the BET surface area results obtained from N_2 adsorption-desorption analysis. The crystal structures of the synthesised N-rich CN samples were confirmed by XRD analysis. The MCN-TMA-x mimics crystal structure of bulk-CN as evident from similar XRD patterns. C_3N_5 exhibited a sharp peak at ~27.6° (d = 0.32 nm) and a small broad hump at ~ 13.10°, which may be assigned to the (002) and (100) crystal planes of the graphitic polymeric CN structure [32] (Fig. 1e). After the formation of mesopores in the C_3N_5 system, the (002) peak position of MCN-TMA-6 was slightly shifted to a lower angle (~27.4°, d = 0.33 nm), and the intensity of both the (002) and (100) peaks was reduced compared with that of Bulk-CN (Fig. 1f). These results contribute to the reduction in long-range ordering by the formation of a mesoporous structure. Lowered diffraction angle suggests increased d spacing in mesoporous C_3N_5. The surface functional groups in the synthesized samples were investigated using FTIR spectroscopy. The FTIR spectra of the MCN-TMA-x samples were found to be similar to those of C_3N_5, as shown in Fig. 1g & S3b. The broad peak between 3100 and 3300 cm^{-1} could be attributed to the residual NH group stretching frequencies, and the shoulder peak around 3500 cm^{-1} was assigned to the -OH stretching vibrational band on the surface of the samples. The strong resonance peaks between 1255 – 1450 cm^{-1} and 1561 cm^{-1} – 1630 cm^{-1} were attributed to the stretching bands of the heterocyclic C-N and C=N bonds in carbon nitride compounds, respectively. The peak at ~806 cm^{-1} can be assigned to the bending vibration band of heterocyclic –C=N– [30,33].

Theoretical studies were conducted to determine the possible C-doping sites in the C_3N_5 structure, as displayed in Fig. 2a, where nitrogen atoms were numbered in the unit cell (dotted red square) to study their substitution with C atoms upon doping. The relative energies of C-doping at different sites are summarised in Table S2, calculated using the generalised gradient approximation method (GGA) using the Perdew-Burke-Ernzerhof (PBE) functional and the hybrid level with the Heyd-Scuseria-Ernzerhof (HSE06) functional. As shown in Table S2 and Fig. 2b, the N7 atom in the fused triazole ring was the most susceptible to substitution because it had the lowest relative free energy level after substitution. Hence, this particular structure was used for further calculations of the C-doped carbon nitride. This is consistent with the positions of the HOMO and LUMO orbitals (Fig. 2c & d), which are congregated around the electron-rich catalytically active edge-sites, while the core carbon and nitrogen atoms remains relatively inert. Furthermore, Bader charges of the pristine and C-doped C_3N_5 are also summarized in Table S3.

NEXAFS analysis was performed to understand the local electronic structures upon carbon doping. The C K-edge and N K-edge (Figs. 3a and 3b) NEXAFS spectra of MCN-TMA-6 exhibited a similar pattern to that of Bulk C_3N_5. In the C K-edge spectra, the strong peak at 288.1 eV could be attributed to the electronic transitions of 1 s orbital to π* (N-C=N) while the broad and small peaks at 284.9 eV and 291.7 eV could be assigned as π* (C=C) and σ* (C-C) transitions [17,34]. In the N K-edge spectra, the strong peak at 399.2 eV is attributed to the π* transition of heterocyclic C-N=C bond while the weak peak at 401.1 eV and strong peak at 402.1 eV corresponds to π* N-3C bonds and sp^3 bridging N atoms [30, 34]. These characteristic peaks suggested the formation of triazole based polymeric C_3N_5 in the synthesized carbon nitride.

XPS analysis was employed to further understand their structural identities. The C1s XPS spectrum of C_3N_5 (Fig. 3c) was deconvoluted to three peak positions centered at the binding energies of 288.0, 285.95, and 284.83 eV, respectively. The prominent peak at 288.0 eV was attributed to the sp^2 hybridized N-C=N in heptazine units in the carbon nitride framework, while the peak at 284.83 eV could be assigned to the graphitic C=C bond, and the weak peak at 285.95 eV corresponded to carbon in the $C-NH_2$ species [35]. The peak area corresponding to the C=C bond in the C1s spectrum of MCN-TMA-6 (27.25 %) was higher than that of intact C_3N_5, and the details are summarised in Table S4. This might be attributed to the presence of extended C=C conjugated bonding in the heterocyclic ring of the CN framework compared to C_3N_5 potentially due to C-doping [36]. The N1s spectra of C_3N_5 and MCN-TMA-6 were deconvoluted into two peaks, as shown in Fig. 3e & f. A strong peak at 398.45 eV could be assigned to the presence of a nitrogen atom neighbouring two carbon atoms (C-N=C) in the heptazine-based framework. The peak centred at 399.87 eV originated from the presence of triazine and triazole moieties, $C-N=N-C/C-NH_2$ of N-rich CN. N1s spectrum of MCN-TMA-6 also exhibited the 2
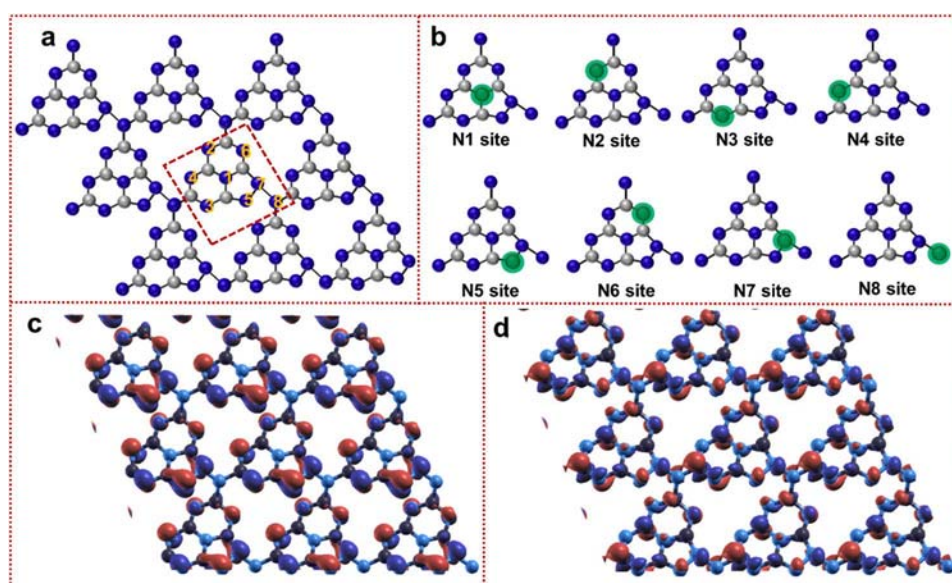

Fig. 2. (a) A top view of the structure of C_3N_5 showing the number of N atoms when considering C-doping, and (b) eight possible N sites were replaced by C-doping structures, where blue and grey represent the N and C atoms, and grey with red outlines (highlightened) represent the dopant and carbon, respectively; (c) HOMO and (d) LUMO orbitals of the C_3N_5 system show that the core is mostly inert.
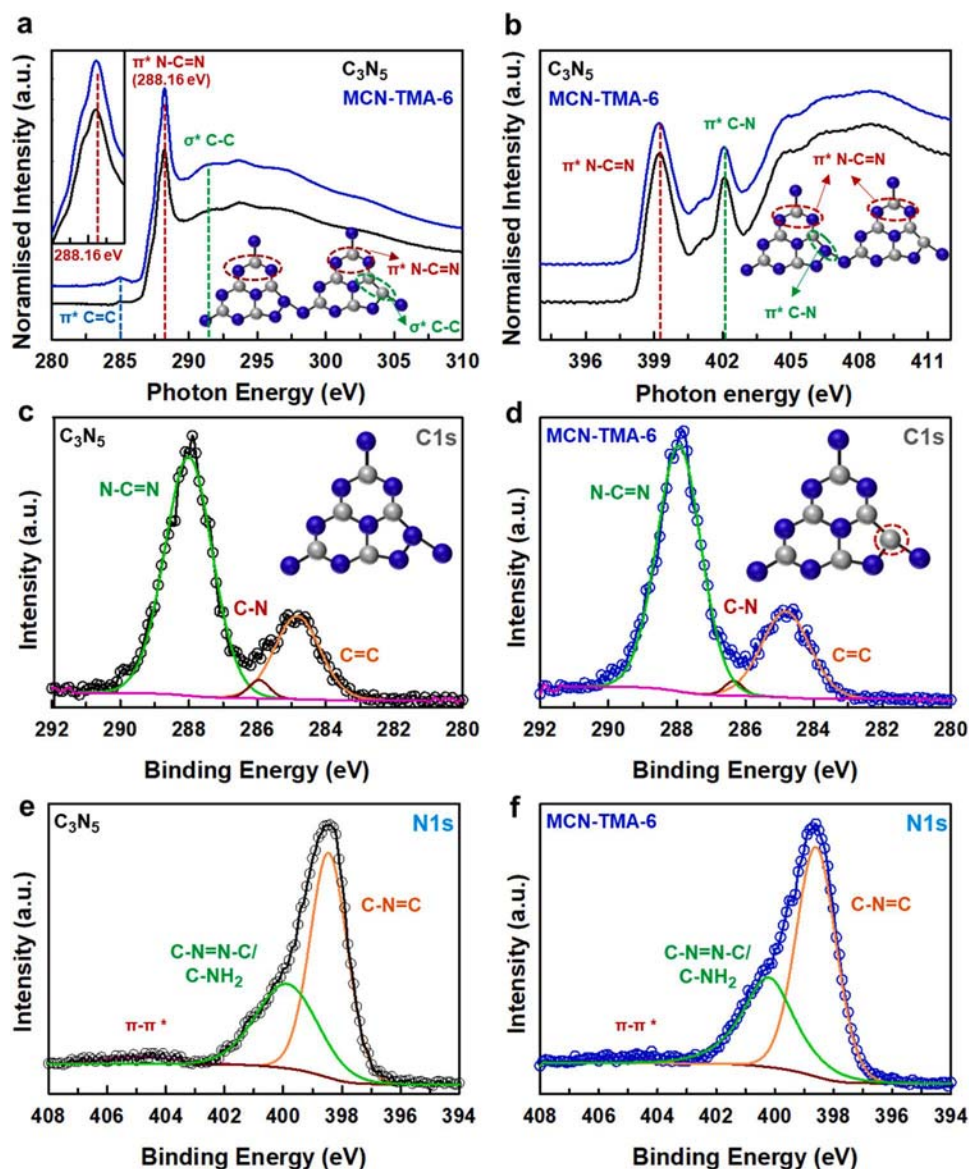
Fig. 3. (a) C K-edge and (b) N K-edge NEXAFS spectra of C_3N_5 and MCN-TMA-6, (c & d) C1s XPS spectra of C_3N_5 and MCN-TMA-6 and (e & f) N1s XPS spectra of C_3N_5 and MCN-TMA-6, respectively.

deconvoluted peaks at 398.59 eV (C-N=C), and 400.4 eV (C-N=N-C/C-NH$_2$). Interestingly, the peak intensity of C-N=N-C/C-NH$_2$ for MCN-TMA-6 was lower than that of C_3N_5 (Table. S4), indicating that some of the N atoms in the triazole ring were replaced with carbon rather than N atoms in the C=N-C triazine ring, [34,37,38] which again proves C-doping and interestingly is in good agreement with the DFT calculations. Additionally, according to CHNS analysis, the stoichiometric N/C ratio of bulk C_3N_5 was calculated to be 1.56 ($C_3N_{4.7}$), while doping the N/C ratio reduces to 1.53 in MCN-TMA-6 ($C_3N_{4.6}$), indicating the substitution of some of the N atoms with C atoms.

UV–Vis absorption spectroscopy analysis was performed to understand the optical properties of the prepared samples (Fig. S4). The characteristic absorption peak around 373 nm for all the samples was attributed to the π-π* electronic transition in the conjugated heterocyclic ring of carbon nitride [39]. MCN-TMA-0 and MCN-TMA-6 exhibited increased absorbance compared to C_3N_5 due to the mesoporosity, carbon doping of CN and crystal defects generation therein, resulting in enhanced light-harvesting properties (Fig. 4a). Additionally, the absorption spectra of the carbon-doped samples (MCN-TMA-x) exhibited a

red-shift in the absorption edge from 478 to 542 nm (Fig. S4) with increasing the amount of the C-doping [40]. The bandgap energy was calculated via the plot between (KM·hν)$^{0.5}$ *vs* the photon energy, as shown in the inset of Fig. 4a. The bandgap energies of C_3N_5 and MCN-TMA-6 were determined to be 2.30 eV and 2.18 eV respectively, which closely aligned with theoretically calculated values, 2.31 eV and 2.14 eV with indirect bandgap, respectively, according to the projected density of states (PDOS) for the proposed structure (Fig. S5).

To understand the recombination of photoinduced charge carriers under light irradiation, photoluminescence spectroscopic analysis was conducted. The PL spectra of the samples are shown in Fig. 4b, where the excitation wavelength is 380 nm. The PL spectrum of C_3N_5 exhibited a strong and broad peak at 468 nm. However, the introduction of mesoporosity in CN (MCN-TMA-0) significantly reduced the PL intensity, which was attributed to the fast transfer of photoinduced electrons to the porous surface, resulting in the suppression of electron-hole recombination kinetics [41,42]. Additionally, the peak position was observed at a higher wavelength (527 nm), indicating the formation of a lower electronic energy level in the CN. Furthermore, C-doping in mesoporous CN (MCN-TMA-6) additionally decreased the PL intensity at 529 nm,
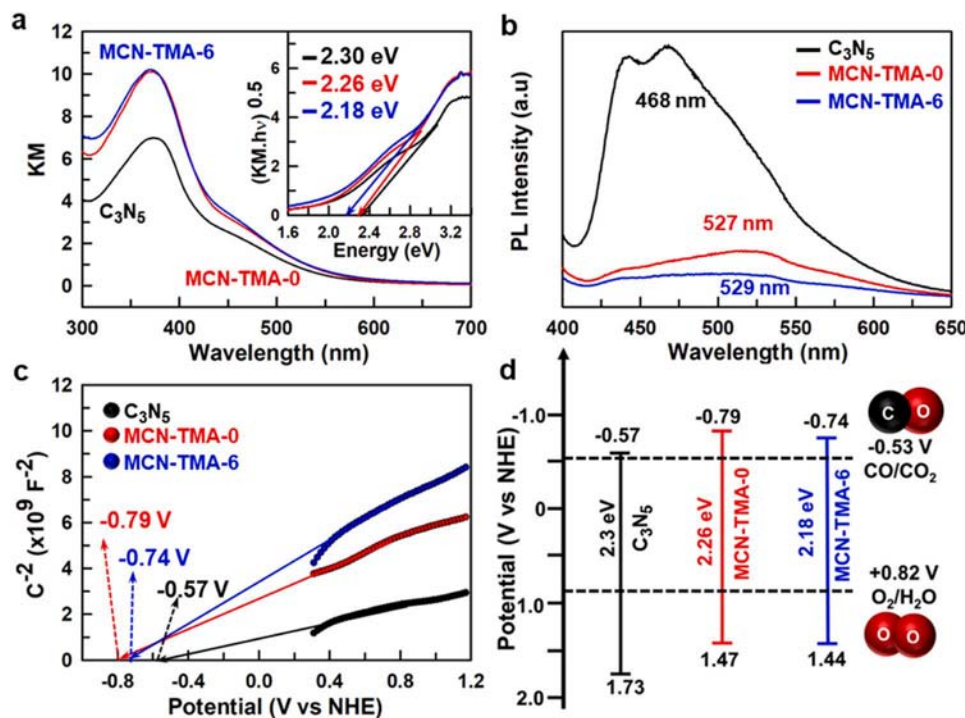
Fig. 4. (a) UV-Vis KM spectra and their Tauc plot (inset); (b) PL spectra, (c) Mott-Schottky plot (2700 Hz), (d) the band diagram of C_3N_5, MCN-TMA-0 and MCN-TMA-6.

which was attributed to the extended π-electron conjugation.

In order to understand the band structure of the prepared CN samples, the conduction band (CB) minimum of the prepared materials was evaluated from Mott-Schottky plots (Fig. 4c and S6) using a three-electrode system under various frequencies including 2700 Hz, 2400 Hz and 2100 Hz at 0 V (*vs* Ag/AgCl further converted to vs NHE). The CB minimum positions of mesoporous samples MCN-TMA-0 (-0.74 V) and MCN-TMA-6 (-0.79 V) were more negative than those of C_3N_5 (-0.57 V vs NHE). However, the CB minimum positions of all materials are still sufficient to reduce CO_2 to CO [11]. The valence band (VB) maximum position can be calculated by subtracting E_g (bandgap energy) from the position of the CB minimum and displayed in Fig. 4d. The VB potentials of C_3N_5, MCN-TMA-0 and MCN-TMA-6 were determined as +1.73 V, +1.47 V, and +1.44 V vs NHE, respectively, indicating that the introduction of porosity and C-doping into the C_3N_5 system can significantly modulate the electronic band structure in a tunable manner. The CB positions of the prepared CNs were more negative than the CO_2 reduction potential, whereas their VB positions were more positive than the water oxidation potential. Additionally, their photoelectrochemical properties were analysed by the photocurrent measurement (Fig. S7a) and Nyquist plots (Fig. S7b) were measured using 0.2 M Na_2SO_4 (aq) electrolyte. MCN-TMA-6 demonstrated a notably higher photocurrent density (5.5 μA/cm²) under the irradiation of visible light (300 W Xe lamp, λ ≥ 400 nm) compared to MCN-TMA-0 (4.9 μA/cm²) and C_3N_5 (0.52 μA/cm²), at zero potential (vs Ag/AgCl electrode). Furthermore, the Nyquist plot reveals that the order of impedance is C_3N_5 > MCN-TMA-0 > MCN-TMA-6. These results suggest that MCN-TMA-6 effectively transferred the photoinduced electrons to the electrodes owing to its enhanced conductivity compared to C_3N_5. As a result, it is expected that the enhanced mesoporosity and conductivity of the CN system (MCN-TMA-6) can deliver superior photocatalytic CO_2 reduction compared to pristine bulk C_3N_5.

The photocatalytic performances of the synthesised samples for CO_2 reduction reaction were evaluated under the visible light irradiation (300 W Xe lamp, λ ≥ 400 nm) with a closed circulation system. The reaction condition set as follows, prepared photocatalyst (30 mg) was dispersed in 11 mL of an organic–aqueous solution containing 9 mL acetonitrile, 1 mL water and 1 mL triethanolamine (TEOA), where triethanolamine is used as hole scavenger. Additionally, 5 μmol of Co(bpy)$_3^{2+}$ was added into the suspension as a co-catalyst. All samples exhibited the photocatalytic CO_2 reduction to CO in the reaction condition as shown in Fig. 5a, and the results were summarized in Table S5. The total evolution amount of CO over 8 h and the time-course curves of CO evolution for the prepared samples are plotted in Fig. 5b-c & Fig. S8. The N-rich carbon nitride (C_3N_5, 28.3 μmol·g⁻¹) produced 2.9 times higher amount of CO than g-C_3N_4 (9.6 μmol·g⁻¹), which could be attributed to the improved visible-light harvesting ability of C_3N_5 and the higher CO_2 adsorption property due to more N sites [43]. According to CO_2 adsorption analyses, displayed in Fig. S9 and summarized in Table S6. MCN-TMA-6, mesoporous C-doped C_3N_5, exhibited a CO_2 adsorption capacity of 1.3 mmol/g, representing 1.09 and 1.83 times higher CO_2 adsorption affinity than those of MCN-TMA-0 and C_3N_5, respectively at 25 °C and 30 bar. Furthermore, the activity of MCN-TMA-6 was also evaluated without a co-catalyst ([Co(bpy)$_3$]$^{2+}$) or a sacrificial reagent (TEOA). As summarized in Table S7, MCN-TMA-6 with [Co(bpy)$_3$]$^{2+}$ produced 8.8 μmol·g⁻¹ of CO over 8 h in the mixed solution of water and acetonitrile (without a sacrificial agent) under visible light while it produced 15.1 μmol·g⁻¹ of CO in the mixed solution of water, acetonitrile and TEOA. However, its photocatalytic CO evolution significantly increased to 116.6 μmol·g⁻¹ in the presence of both [Co(bpy)$_3$]$^{2+}$ and TEOA.

In addition, P25 (TiO_2 nanoparticle) as a control sample did not exhibit the conversion of CO_2 under visible light irradiation in this condition due to the large band gap (~3.2 eV). However, MCN-TMA-0, which has a mesoporous structure, produced 79.6 μmol·g⁻¹ of CO in 8 h, which is 2.8 times enhanced performance than that of C_3N_5. This enhancement could be attributed to the improved surface active sites and enhanced visible light harvesting. Furthermore, MCN-TMA-6 exhibited the highest CO evolution of 116.6 μmol·g⁻¹, which is 4-fold enhanced performance compared to C_3N_5. This significantly enhanced performance in photocatalytic CO_2 conversion could be attributed to the synergistic effect of the porosity, enhanced light absorption property,
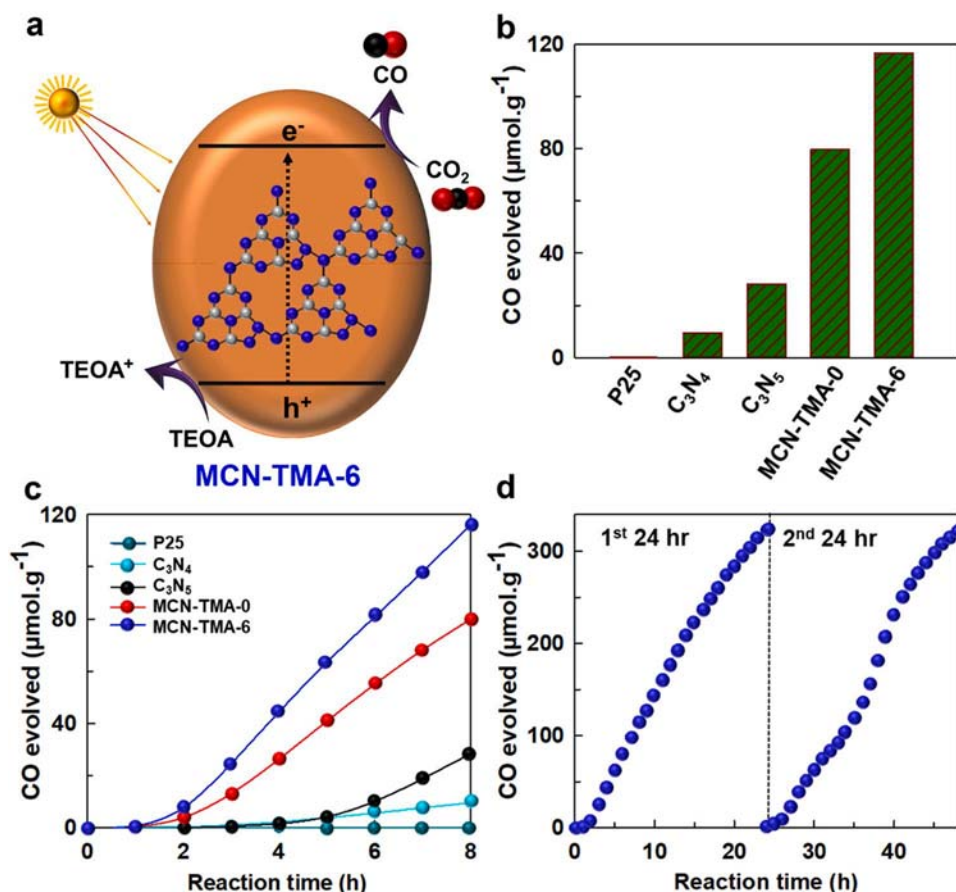
Fig. 5. (a) Schematic representation for photocatalytic CO_2 reduction of MCN-TMA, (b) the amount of evolved CO via the photocatalytic reaction in 8 h, (c) the time-course plot of CO evolution for P25, C_3N_4, C_3N_5 and MCN-TMAs and (d) the long-term stability test of the optimised sample under the visible light irradiation ($\lambda \geq 400$ nm).

and engineered band structure by carbon doping. Moreover, the photocatalytic enhancement of MCN-TMA-6 might also be attributed to the highly suppressed exciton recombination kinetics and improved electrical conductivity, resulting in efficient electron transfer to the surface-active sites, as demonstrated by the PL and impedance analyses. However, highly C-doped mesoporous C_3N_5 exhibited a decreased photocatalytic CO_2 conversion performance owing to the light-shielding effect of excessive C-doping [44]. According to gas chromatography analysis, all the prepared photocatalysts mostly converted CO_2 to CO, while only a negligible trace of methane was detected within 8 h. Furthermore, we conducted control experiments including Ar atmosphere without CO_2 to indirectly verify the origin of the detected CO, which were summarized in Table S7. In the optimal photocatalytic reaction condition without CO_2, any CO was not produced, confirming that the CO produced by MCN-TMA-6 in the photocatalytic reaction originated from the supplied CO_2 gas. In addition, the long-term stability of MCN-TMA-6 photocatalyst was tested via two consecutive 24 h photocatalytic reactions, equivalent to 6 cycles. As shown in Fig. 5d, MCN-TMA-6 produced 323.16 $\mu mol \cdot g^{-1}$ of CO in the first 24 h, which did not significantly deviate from the estimated value (349.8 $\mu mol \cdot g^{-1}$) based on the performance observed over an 8 h period, as shown in Fig. 5c. Moreover, during the second 24 h photocatalytic reaction, 323.13 $\mu mol \cdot g^{-1}$ of CO was produced from CO_2, indicating that the photocatalytic CO_2 conversion performance has retained 92 % efficiency over 48 h. Furthermore, the structural stability of MCN-TMA-6 photocatalyst was evaluated using XRD and TEM analyses before and after the photocatalytic CO_2RR as demonstrated in Fig. S10. The XRD patterns before and after the reaction (Fig. S10a), exhibited no significant changes in peak position or broadness. Additionally, the TEM image of MCN-TMA-6

(Fig. S10b) after the reaction showed similar porous texture to that observed before the reaction (Fig. 1d). These results suggest that the developed MCN-TMA-6 retains its intact crystal structure with mesopore and sustainably converts CO_2 to CO continuously via photocatalytic process, making notable advancements over other reported CN-based catalysts (Table S8).

The enhanced photocatalytic activity of the material also was confirmed by the DFT calculation. The photocatalytic reduction of CO_2 proceeds through the intermediate COOH* [45,46], as shown in Fig. 6a & b. Initially, active H* must be present on the catalyst under the illumination. We observe that the H* (electrophile) is bound too strongly on the pristine structure to allow for CO_2 reduction, while the C-doped structure is better suited due to the weaker interaction. On the other hand, the adsorption of OH* (nucleophile) is improved upon doping. This has consequences for the rate-determining step. Then, COOH is formed as activated H* is transferred from the nitrogen atom to CO_2. In the second reaction step, the C-O bond is cleaved, and CO is formed. Ultimately, H_2O is released as another H* is transferred from the adjacent nitrogen atom. Comparing the reaction mechanism on the pristine and C-doped structure, the beneficial effect of C-doping is revealed in three ways: (i) decreased excitation energies, (ii) lowered reaction barriers due to weaker binding of H* to the catalyst, (iii) reduced CO binding to the catalyst, preventing the formation of inert spectator species or catalyst poisoning. Instead, a highly active H* is present and CO* readily dissociates after the reaction is finished. The adsorption energies of H* (relative to ½ H_2) and CO* are 1.56 eV and 1.03 eV, respectively, on the pristine structure and 1.06 eV and 0.13 eV on the C-doped structure.
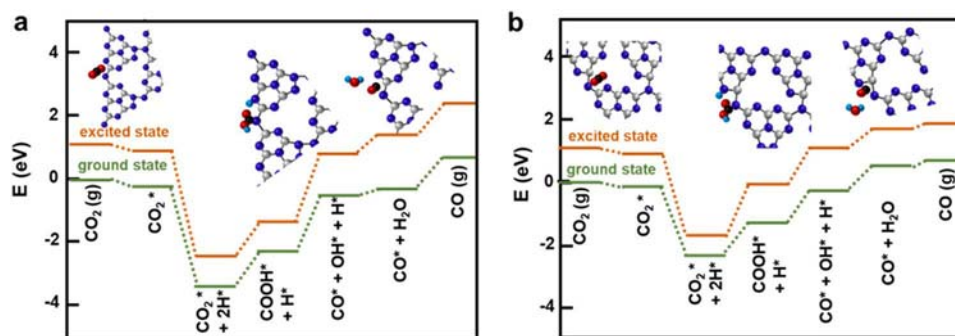
Fig. 6. The potential energy landscape for CO_2 reduction to CO in the ground state (DFT) and in the excited state (TD-DFT) under illumination on (a) pristine C_3N_5 and (b) C-doped C_3N_5. The excited state corresponds to the first (lowest) excitation, as calculated with TD-DFT.

4. Conclusion

In summary, we developed a novel mesoporous C-doped N-rich carbon nitride photocatalyst with a high CO_2 conversion efficiency. N_2 adsorption-desorption isotherm analysis and TEM analysis demonstrated that MCN-TMA-6 exhibited a high surface area (64 m^2g^{-1}) and a desired pore size of $\sim$ 12 nm. More interestingly, UV-Vis, PL, and impedance analyses revealed that the introduction of C-doping in an N-rich carbon nitride structure reduced the bandgap energy, enhanced conductivity, and suppressed electron-hole recombination kinetics. The electron-rich N sites in the N-rich carbon nitride acted as active sites for the adsorption of CO_2 molecules and their catalytical conversion to CO. The C-doped mesoporous CN exhibited superior photocatalytic CO_2 conversion performance with CO evolution of 116.6 $\mu mol \cdot g^{-1}$ in 8 h under visible light irradiation, which is 4.1 times higher than that of C_3N_5 and 12.1 times higher than that of g-C_3N_4. Furthermore, the recyclability test revealed that MCN-TMA-6 sustainably converted CO_2 to CO without a significant reduction in conversion efficiency. Additionally, theoretical calculations revealed that C-doping in carbon nitride structure decreased the bandgap energy, was energetically favourable for the photocatalytic reaction and allowed easier desorption of the products. The photocatalytic reaction proceeded through the COOH intermediate, which was decomposed into CO and H_2O with high selectivity towards CO. Due to these advantages, C-doped N-rich carbon nitrides can efficiently reduce CO_2 to CO compared to the pristine carbon nitride. Furthermore, they can also be applied to various photocatalytic applications like photocatalytic pollutant degradation for water purification, water splitting, nitrogen reduction, and so on.

Authorship contribution statement

A.M.S performed most of the experiments, data analysis and writing and editing. M.F helped in experiments and data analysis. N.P.D helped in physical characterization of materials, reviewed and edited. M. H performed the theoretical calcualtion and data analysis. G.S reviewed and edited. C.I.S helped physical characterization of materials. B.L superivised theoretical calcualtion. Z.L helped in TEM analysis. A.M.R helped physical characterization of materials. C.H.J reviewed and edited. J.H.Y designed experiments and co-supervised, reviewed and edited. P.K guided, reviewed and edited. A.V reviewed, edited and supervised the research.

Declaration of Competing Interest

The authors declare that they have no known competing financial interests or personal relationships that could have appeared to influence the work reported in this paper.

Acknowledgements

Appendix A. Supporting information

Supplementary data associated with this article can be found in the online version at doi:10.1016/j.apcatb.2024.124701.

Data Availability

Data will be made available on request.

References

[1] M. Hertzberg, H. Schreuder, Role of atmospheric carbon dioxide in climate change, Energy Environ. 27 (2016) 785–797.

[2] R. Lindsey, and L. Dahlman, https://www.climate.gov/news-features/understanding-climate/climate-change-global-temperature, NOAA Climate, SCIENCE & INFORMATION FOR A CLIMATE-SMART NATION, Jan 18, 2024.

[3] J. Ma, N. Sun, X. Zhang, N. Zhao, F. Xiao, W. Wei, Y. Sun, A short review of catalysis for CO_2 conversion, Catal. Today 148 (2009) 221–231.

[4] I. Sullivan, A. Goryachev, I.A. Digdaya, X. Li, H.A. Atwater, D.A. Vermaas, C. Xiang, Coupling electrochemical CO_2 conversion with CO_2 capture, Nat. Catal. 4 (2021) 952–958.

[5] S.L. Hou, J. Dong, X.Y. Zhao, X.S. Li, F.Y. Ren, J. Zhao, B. Zhao, Thermocatalytic conversion of CO_2 to valuable products activated by noble-metal-free metal-organic frameworks, Angew. Chem. Int. Ed. (2023) e202305213.

[6] K.-Y. Tao, K. Yuan, W. Yang, D.-C. Zhong, T.-B. Lu, A template co-pyrolysis strategy towards the increase of amino/imino content within g-C_3N_4 for efficient CO_2 photoreduction, Chem. Eng. J. 455 (2023) 140630.

[7] Y. Wang, E. Chen, J. Tang, Insight on reaction pathways of photocatalytic CO_2 conversion, ACS Catal. 12 (2022) 7300–7316.

[8] Y. Li, D. Hui, Y. Sun, Y. Wang, Z. Wu, C. Wang, J. Zhao, Boosting thermo-photocatalytic CO_2 conversion activity by using photosynthesis-inspired electron-proton-transfer mediators, Nat. Commun. 12 (2021) 123.

[9] Y.-N. Gong, B.-Z. Shao, J.-H. Mei, W. Yang, D.-C. Zhong, T.-B. Lu, Facile synthesis of C_3N_4-supported metal catalysts for efficient CO_2 photoreduction, Nano Res 15 (2022) 551–556.

[10] S. Hu, P. Qiao, X. Yi, Y. Lei, H. Hu, J. Ye, D. Wang, Selective photocatalytic reduction of CO_2 to CO mediated by silver single atoms anchored on tubular carbon nitride, Angew. Chem. Int. Ed. 62 (2023) e202304585.

[11] A.M. Sadanandan, J.-H. Yang, V. Devtade, G. Singh, N.P. Dharmarajan, M. Fawaz, J.M. Lee, E. Tavakkoli, C.-H. Jeon, P. Kumar, Carbon nitride based nanoarchitectonics for nature-inspired photocatalytic CO_2 reduction, Prog. Mater. Sci. (2024) 101242.

[12] J. Low, B. Cheng, J. Yu, Surface modification and enhanced photocatalytic CO_2 reduction performance of TiO_2: a review, Appl. Surf. Sci. 392 (2017) 658–686.

[13] H. Takeda, O. Ishitani, Development of efficient photocatalytic systems for CO_2 reduction using mononuclear and multinuclear metal complexes based on mechanistic studies, Coord. Chem. Rev. 254 (2010) 346–354.

[14] S.N. Talapaneni, G. Singh, I.Y. Kim, K. AlBahily, et al., Nanostructured carbon nitrides for CO_2 capture and conversion, Adv. Mater. 32 (2020) 1904635.

[15] M. Fawaz, R. Bahadur, N.P. Dharmarajan, J.-H. Yang, C. Sathish, A.M. Sadanandan, V. Perumalsamy, G. Singh, X. Guan, P. Kumar, Emerging trends of carbon nitrides and their hybrids for photo-/electro-chemical energy applications, Carbon 214 (2023) 118345.

[16] N.P. Dharmarajan, D. Vidyasagar, J.H. Yang, S.N. Talapaneni, J. Lee, K. Ramadass, G. Singh, M. Fawaz, P. Kumar, A. Vinu, Bio-inspired supramolecular self-assembled carbon nitride nanostructures for photocatalytic water splitting, Adv. Mater. 36 (2024) 2306895.

[17] G.P. Mane, S.N. Talapaneni, K.S. Lakhi, H. Ilbeygi, U. Ravon, K. Al-Bahily, T. Mori, D.H. Park, A. Vinu, Highly ordered nitrogen-rich mesoporous carbon nitrides and their superior performance for sensing and photocatalytic hydrogen generation, Angew. Chem. Int. Ed. 56 (2017) 8481–8485.

[18] K. Qi, S.-y Liu, A. Zada, Graphitic carbon nitride, a polymer photocatalyst, J. Taiwan Inst. Chem. Eng. 109 (2020) 111–123.

[19] A. Zhu, L. Qiao, P. Tan, J. Pan, Interfaces of graphitic carbon nitride-based composite photocatalysts, Inorg. Chem. Front. 7 (2020) 4754–4793.

[20] P. Kumar, G. Singh, X. Guan, J. Lee, R. Bahadur, K. Ramadass, P. Kumar, M. G. Kibria, D. Vidyasagar, J. Yi, Multifunctional carbon nitride nanoarchitectures for catalysis, Chem. Soc. Rev. 52 (2023) 7602–7664.

[21] B. Debnath, S. Singh, S.M. Hossain, S. Krishnamurthy, V. Polshettiwar, S. Ogale, Visible light-driven highly selective CO_2 reduction to CH_4 using potassium-doped g-C_3N_5, Langmuir 38 (2022) 3139–3148.

[22] Y. Wang, T.N. Pham, Y. Tian, Y. Morikawa, L. Yan, Density functional theory study on a nitrogen-rich carbon nitride material C_3N_5 as photocatalyst for CO_2 reduction to C1 and C2 products, J. Colloid Interface Sci. 585 (2021) 740–749.

[23] G. Kresse, J. Hafner, Ab initio molecular dynamics for liquid metals, Phys. Rev. B. 47 (1993) 558.

[24] G. Kresse, J. Furthmüller, Efficiency of ab-initio total energy calculations for metals and semiconductors using a plane-wave basis set, Comput. Mater. Sci. 6 (1996) 15–50.

[25] G. Kresse, J. Furthmüller, Efficient iterative schemes for ab initio total-energy calculations using a plane-wave basis set, Phys. Rev. B. 54 (1996) 11169.

[26] G. Kresse, D. Joubert, From ultrasoft pseudopotentials to the projector augmented-wave method, Phys. Rev. B. 59 (1999) 1758.

[27] J.P. Perdew, K. Burke, M. Ernzerhof, Generalized gradient approximation made simple, Phys. Rev. Lett. 77 (1996) 3865.

[28] S. Grimme, J. Antony, S. Ehrlich, H. Krieg, A consistent and accurate ab initio parametrization of density functional dispersion correction (DFT-D) for the 94 elements H-Pu, J. Chem. Phys. 132 (2010).

[29] A.V. Krukau, O.A. Vydrov, A.F. Izmaylov, G.E. Scuseria, Influence of the exchange screening parameter on the performance of screened hybrid functionals, J. Chem. Phys. 125 (2006).

[30] J.-H. Yang, S. Kim, I.Y. Kim, J.M. Lee, J. Yi, A. Karakoti, S. Joseph, K. Albahily, A. Vinu, Highly enhanced photocatalytic hydrogen evolution activity of graphitic carbon nitride with 3D connected mesoporous structure, Sustain. Mater. Technol. 25 (2020) e00184.

[31] Y. Ma, Z. Wang, X. Xu, J. Wang, Review on porous nanomaterials for adsorption and photocatalytic conversion of CO_2, Chin. J. Catal. 38 (2017) 1956–1969.

[32] E. Alwin, W. Nowicki, R. Wojcieszak, M. Zieliński, M. Pietrowski, Elucidating the structure of the graphitic carbon nitride nanomaterials via X-ray photoelectron spectroscopy and X-ray powder diffraction techniques, Dalton Trans. 49 (2020) 12805–12813.

[33] K. He, J. Xie, M. Li, X. Li, In situ one-pot fabrication of g-C_3N_4 nanosheets/NiS cocatalyst heterojunction with intimate interfaces for efficient visible light photocatalytic H_2 generation, Appl. Surf. Sci. 430 (2018) 208–217.

[34] I.Y. Kim, S. Kim, X. Jin, S. Premkumar, G. Chandra, N.S. Lee, G.P. Mane, S. J. Hwang, S. Umapathy, A. Vinu, Ordered mesoporous C_3N_5 with a combined triazole and triazine framework and its graphene hybrids for the oxygen reduction reaction (ORR), Angew. Chem. 130 (2018) 17381–17386.

[35] J. Fang, H. Fan, M. Li, C. Long, Nitrogen self-doped graphitic carbon nitride as efficient visible light photocatalyst for hydrogen evolution, J. Mater. Chem. 3 (2015) 13819–13826.

[36] Y. Li, S. Wu, L. Huang, J. Wang, H. Xu, H. Li, Synthesis of carbon-doped g-C_3N_4 composites with enhanced visible-light photocatalytic activity, Mater. Lett. 137 (2014) 281–284.

[37] Y. Jiang, Z. Sun, C. Tang, Y. Zhou, L. Zeng, L. Huang, Enhancement of photocatalytic hydrogen evolution activity of porous oxygen doped g-C_3N_4 with nitrogen defects induced by changing electron transition, Appl. Catal. B. 240 (2019) 30–38.

[38] J. Zhang, B. Jing, Z. Tang, Z. Ao, D. Xia, M. Zhu, S. Wang, Experimental and DFT insights into the visible-light driving metal-free C_3N_5 activated persulfate system for efficient water purification, Appl. Catal. B. Environ. 289 (2021) 120023.

[39] N. Prakash, G. Kumar, M. Singh, A. Barvat, P. Pal, S.P. Singh, H. Singh, S. P. Khanna, Binary multifunctional ultrabroadband self-powered g-C_3N_4/Si heterojunction high-performance photodetector, Adv. Opt. Mater. 6 (2018) 1800191.

[40] Z. Chen, T.-T. Fan, X. Yu, Q.-L. Wu, Q.-H. Zhu, L.-Z. Zhang, J.-H. Li, W.-P. Fang, X.-D. Yi, Gradual carbon doping of graphitic carbon nitride towards metal-free visible light photocatalytic hydrogen evolution, J. Mater. Chem. A 6 (2018) 15310–15319.

[41] A. Hayat, F. Raziq, M. Khan, J. Khan, S.K.B. Mane, A. Ahmad, M.U. Rahman, W. U. Khan, Fusion of conjugated bicyclic co-polymer within polymeric carbon nitride for high photocatalytic performance, J. Colloid Interface Sci. 554 (2019) 627–639.

[42] S. Zhao, Y. Zhang, J. Fang, H. Zhang, Y. Wang, Y. Zhou, W. Chen, C. Zhang, Self-assembled mesoporous carbon nitride with tunable texture for enhanced visible-light photocatalytic hydrogen evolution, ACS Sustain. Chem. Eng. 6 (2018) 8291–8299.

[43] D.H. Park, K.S. Lakhi, K. Ramadass, M.K. Kim, S.N. Talapaneni, S. Joseph, U. Ravon, K. Al-Bahily, A. Vinu, Energy efficient synthesis of ordered mesoporous carbon nitrides with a high nitrogen content and enhanced CO_2 capture capacity, Chem. A Eur. J. 23 (2017) 10753–10757.

[44] M. Sun, Y. Zhou, T. Yu, Synthesis of g-C_3N_4/NiO-carbon microsphere composites for Co-reduction of CO_2 by photocatalytic hydrogen production from water decomposition, J. Clean. Prod. 357 (2022) 131801.

[45] H. Zhao, L. Liu, J.M. Andino, Y. Li, Bicrystalline TiO_2 with controllable anatase–brookite phase content for enhanced CO_2 photoreduction to fuels, J. Mater. Chem. A. 1 (2013) 8209–8216.

[46] L. Liu, C. Zhao, Y. Li, Spontaneous dissociation of CO_2 to CO on defective surface of Cu (I)/TiO_{2-x} nanoparticles at room temperature, J. Phys. Chem. C. 116 (2012) 7904–7912.